Numerical calculation of transverse coupling impedances: Comparison to Spallation Neutron Source extraction kicker measurements

B. Doliwa, E. Arévalo, and T. Weiland

TEMF, Technische Universität Darmstadt, Schlossgartenstrasse 8, D-64289 Darmstadt, Germany
(Received 6 February 2007; published 22 October 2007)

The study of beam dynamics and the localization of potential sources of instabilities are important tasks in the design of modern, high-intensity particle accelerators. In the case of synchrotrons and storage rings, coupling impedance data are needed to characterize the parasitic interaction of critical components with the beam. In this article we demonstrate the application of numerical field simulations to the computation of transverse kicker coupling impedances. Based on the 3D simulation results, a parametrized model is developed to incorporate the impedance of an arbitrary pulse-forming network attached to the kicker. Detailed comparisons of numerical results with twin-wire and direct measurements are discussed at the example of the Spallation Neutron Source extraction kicker.

I. INTRODUCTION

The electromagnetic interaction of an intense charged particle beam with its vacuum chamber surroundings in an accelerator plays an important role for the study of beam dynamics and collective beam instabilities [1]. The so-called wakefields generated by particles moving through an accelerator component such as kickers affect the motion of the following particles in the beam, and may cause the loss of particles, beam energy spread, and instabilities. In order to avoid collective beam instabilities that limit the accelerator performance, an accurate numerical description of the effect of wakefields on the beam is necessary.

Obviously, the description of the full physical problem—the self-consistent motion of a large number of classical, charged particles interacting with the accelerator and with each other—is rather complex. For very dilute beams, the direct electromagnetic interaction between particles can be neglected against the steering external fields imposed by the accelerator, implying that a single-particle picture is sufficient for computing trajectories. Upon going to higher intensities, direct (so-called space-charge) interactions and wakefield effects become relevant. Models for the former are usually built directly into the beam-dynamics simulations. The characterization of wakefield effects is most easily achieved in a two-particle picture: A first, source particle excites electromagnetic fields in an accelerator component. A second, test particle interacts with the fields and thus suffers a certain momentum change which depends on the distance to the first particle and further parameters, like axis offsets. Instead of solving the equations of motion for these particles, fixed, straight trajectories are assumed as a further simplification (the rigid-beam approximation).

In the case of synchrotrons and storage rings, wakefield effects are most conveniently described in the frequency domain, leading to the concept of coupling impedances (see Sec. II). As coupling impedances are given by the complex electromagnetic interaction of beam particles with the accelerator components, beam-dynamics simulations do normally not incorporate the respective models, but require the coupling impedance data from a separate source. Having in mind that analytical calculations are not able to cope with the geometrical complexity of a typical accelerator component like a kicker, and that measurements have the drawback of needing prototypes, we will demonstrate in this work that numerical field calculations offer a convenient alternative to obtain coupling impedance data.

In this paper, for brevity, we consider only *transverse* coupling impedances. In Sec. II, we will review their definition and discuss the twin-wire approximation that is used in the simulations. In Sec. III, the essential features of our numerical approach will be discussed, including the procedure used to incorporate into the simulations the external pulse-forming network (PFN) of a kicker. In Sec. IV, we will introduce a parametrized model for the PFN influence on transverse kicker impedances. One module of a kicker used in the Spallation Neutron Source (SNS) accumulator ring [2], will be treated as an example in Sec. V. In particular, we will compare our numerical results with the detailed measurements performed by Davino and Hahn on a prototype [3–6]. In Sec. VI, we will give a summary and conclusions.

II. TRANSVERSE COUPLING IMPEDANCE

A. Definition

We follow the notation of Refs. [1,7]. The vertical coupling impedance in the Cartesian coordinate system is defined by

$$Z_y(\omega) \equiv \frac{\mathrm{i}}{q\Delta} \int_{-\infty}^{\infty} \mathrm{d}z (E_y + \beta c B_x) e^{\mathrm{i}kz}, \qquad (1)$$

where z is the beam direction, and x and y are the horizontal and vertical directions, respectively. In Eq. (1) the

particles move in the z-direction with velocity βc, and $k = \omega/\beta c$. E_y and B_x are the y-component of the electrical field $[E(x, y, z; \omega)]$ and x-component of the magnetic field $[B(x, y, z; \omega)]$, respectively. The fields are in turn generated by the beam which is modeled as the current density $j(x, y, z; \omega)$, whose components are $j_x = j_y = 0$ and

$$j_z(x, y, z; \omega) = q\delta(x)\delta(y - \Delta)e^{-ikz}. \tag{2}$$

Notice that Eq. (2) describes in the frequency domain a point charge q traveling along the z-axis with velocity βc and vertical offset $y = \Delta$, i.e. $j_z(x, z, y; t) = q\beta c\delta(x)\delta(y - \Delta)\delta(z - \beta ct)$. Here, the offset Δ is essential to the definition of Z_y, as well as the fact that fields in Eq. (1) are evaluated at $x = y = 0$. Analogous expressions can be written down for the horizontal coupling impedance.

We remark that we have adopted a convention where the fields E and B carry the units of Vs/m and Ts, respectively, as they constitute spectral densities. Similarly, $[j] = $ As/m^2, so that Z_y has the unit of Ω/m. The reason for the occurrence of 1/m is that Z_x represents an impedance *per transverse displacement*, Δ: For a small enough Δ, Z_y becomes independent of Δ.

B. Two-wire approximation

Upon using Faraday's law we can rewrite Eq. (1):

$$Z_y(\omega) = \frac{-1}{kq\Delta} \int_{-\infty}^{\infty} dz(\partial_y E_z^+)|_{(0,0,z;\omega)}e^{ikz}, \tag{3}$$

where the "+" superscript reminds us that the excitation current is located at offset $y = +\Delta$. Because of the linearity of Maxwell's equations, we obtain the same expression from a *negative* source term at $y = -\Delta$, leading to the following average:

$$Z_y(\omega) = \frac{-1}{2kq\Delta} \int_{-\infty}^{\infty} dz\partial_y(E_z^+ + E_z^=)|_{(0,0,z;\omega)}e^{ikz}. \tag{4}$$

Here, the two minus signs in the superscript indicate that the corresponding current is at offset $y = -\Delta$ *and* has changed sign. For numerical purposes it is convenient to rewrite Eq. (4) as

$$\begin{aligned} Z_y(\omega) &\approx \frac{-1}{4kq\Delta^2} \int_{-\infty}^{\infty} dz[E_z(0, \Delta, z) - E_z(0, -\Delta, z)]e^{ikz} \\ &= \frac{-1}{4kq^2\Delta^2} \int_V dV E^{(2)} \cdot (j^{(2)})^\star, \end{aligned} \tag{5}$$

where V denotes volume. In order to obtain Eq. (5), the definition of central differences for the term $\partial_y E_z$ was used [7]. In Eq. (5) the field $E^{(2)} \equiv E^+ + E^=$ arises from the excitation of the dipolar current $j^{(2)}$, with components $j_x^{(2)} = j_y^{(2)} = 0$ and

$$j_z^{(2)} = q\delta(x)[\delta(y - \Delta) - \delta(y + \Delta)]e^{-ikz}. \tag{6}$$

Equations (5) and (6) are the two-wire representation of the transverse, vertical coupling impedance. Equation (5) shows why calling Z_y an impedance is plausible, as it is given by an integral over a power density, divided by the current squared [leaving alone the factor $1/(4k\Delta^2)$]. The minus sign ensures that Re$Z_y > 0$ because Re $\int dV E^{(2)} \cdot j^{(2)}$ must always be negative in a passive device—the beam can only lose energy.

Notice also that Eq. (6) represents the twin-wire line inserted in the kicker in the experimental measuring procedure. An example of this setup is given in Sec. V, Fig. 3.

III. NUMERICAL APPROACH

The main task in computing Z_x or Z_y is to solve Maxwell's equations in the frequency domain with the excitation density current $j^{(2)}$. Combining Faraday's and Ampere's laws, one obtains the second-order wave equation for the electric field:

$$\partial \times \mu^{-1}\partial \times E - \omega^2\epsilon E = -i\omega j^{(2)}. \tag{7}$$

Here, ϵ and μ are the permittivity and permeability, respectively, which are functions of both frequency and position. Notice that for $\omega \neq 0$ the solution of Eq. (7) under given boundary conditions is unique.

Although Eq. (7) can be solved analytically in some special cases, complex model geometries necessitate the application of numerical field calculations. In the following we will describe the aspects of our computational approach that are essential to our application. The interested reader is referred to Refs. [8–12] for further details.

A. Equations and discretization

We solve Eq. (7) within the framework of the finite integration technique (FIT) [8,9]. This scheme allows the approximation of Eq. (7) by a system of linear algebraic equations,

$$C^T M_\nu C\widehat{e} - \omega^2 M_\epsilon\widehat{e} = -i\omega\widehat{\widehat{j}}_{\text{ext}}, \tag{8}$$

where the elements $\widehat{e}_i$ of the vector $\widehat{e}$ are the line integrals of the electric field along the edges of a structured, hexagonal grid [13]. The matrix C can be interpreted as a discretized version of the continuous curl operator, whereas the matrices M_ν and M_ϵ reflect the permeability and permittivity, respectively, plus mesh metrics.

Strategies for the efficient solution of (the complex-valued) Eq. (8) are not within the scope of this article; see [10,11].

B. Boundary conditions

In our simulations, the walls of the vacuum vessel containing the kicker module are assumed to be perfectly conducting (i.e. tangential electrical fields vanish on the wall). At the beam-entry and -exit planes, however, special

boundary conditions are needed, which we discuss in the following. Generally, the transitions from the module to the adjacent beam pipe have to be included into the computation, since jumps in pipe cross sections are known to contribute to the coupling impedance. For frequencies below beam-pipe cutoff, the additional field excited within the module decays exponentially into the beam pipe. Thus, at some distance along the beam pipe, the perturbation resulting from the module can be neglected and fields can be considered stationary, i.e. $(E, B)_{\text{pipe}} \propto \exp(-\mathrm{i}kz)$. Using this property, we set up boundary conditions for the 3D problem by solving for $(E, B)_{\text{pipe}}$ in a 2D cross section of the beam pipe (see Sec. V, Fig. 3 for an illustration). A complete discussion of beam-adapted boundary conditions can be found in [14].

C. Modeling of the PFN

So far our code can compute transversal impedances of accelerator components. In the particular case of a ferrite kicker magnet (see Sec. V for details), it is well known that the transverse impedance is strongly influenced by the inductive coupling to the external pulse-forming, network (PFN) [3,4]. We have modeled the PFN in the field simulations as a variable impedance Z_g. This variable impedance is inserted in the FIT mesh of the system [10–12] as follows. We first localize one of the FIT grid edges that joins the two ends of the magnet winding. We then modify the material matrix M_ϵ at the respective component j:

$$(M_\epsilon)_{jj} \rightarrow (M_\epsilon)_{jj} + \frac{1}{\mathrm{i}\omega Z_g(\omega)}. \qquad (9)$$

Note that, for simplicity, this assumes that the winding ends are separated by exactly one grid edge, posing some restriction on possible meshes. An illustration is given in Sec. V, Fig. 3.

D. Implementation

The CAD construction of the kicker model and FIT mesh creation is done using the commercial software CST MICROWAVE STUDIO® [15]. Therein, ferrite parts are modeled with constant, real permeability (to be corrected in the equation setup). The FIT mesh is generated in such a way that two longitudinal mesh lines are present at offsets $(0, \Delta)$ and $(0, -\Delta)$ from the beam axis, facilitating the discretization of the twin-wire excitation, Eq. (6).

The subsequent field computations are performed with a self-implemented electromagnetic solver, along the following steps. (For details of how to carry out this procedure in the FIT framework, the reader is referred to the FIT literature cited in Sec. III A). (i) Mesh information and material data are read from CST MICROWAVE STUDIO®. (ii) The FIT material matrices M_ν and M_ϵ are set up incorporating, first, the frequency-dependent, complex permeability of ferrite parts (different from the original

model), second, the modification equation (9) accounting for the lumped PFN impedance. (iii) The curl operators, C and C^T, are constructed from the mesh incidence information. (iv) The matrix operator of the discrete wave equation (8), i.e. $C^T M_\nu C - \omega^2 M_\epsilon$, is assembled for the given frequency $\omega/2\pi$. Degrees of freedom within perfectly conducting materials are eliminated from the operator. (v) The right-hand side of Eq. (8) is set up as a complex column vector $\widehat{\widehat{\mathbf{j}}}_{\text{ext}}$ representing the discrete approximation of the twin-wire excitation given in Eq. (6). (vi) The beam-adapted boundary conditions (Sec. III B) are enforced by adding their equivalent current densities to the right-hand side of Eq. (8). (vii) Equation (8) is solved for the electrical field $\widehat{\mathbf{e}}$ by an appropriate linear equation solver. This is the most time-consuming step. (viii) The vertical coupling impedance is computed from $\widehat{\mathbf{e}}$ via the FIT-discretized version of Eq. (5):

$$Z_y(\omega) \approx Z_y^{\text{sim}}(\omega) = \frac{-1}{4kq^2\Delta^2} \widehat{\mathbf{e}} \cdot (\widehat{\widehat{\mathbf{j}}}_{\text{ext}})^*. \qquad (10)$$

We have chosen a hybrid-language implementation for our code, using a combination of PYTHON and C + +. Linear-algebra computations are carried out with the help of the Trilinos library [16]. Further details on the simulations are given in [10–12] and references therein.

We note that there exist other possibilities for calculating transversal impedances in particle accelerator components. For instance, they can be calculated by Fourier transformation of wake potentials which in turn can be calculated from wakefield simulations in the time domain [17]. As kicker impedances are of interest down to frequencies below 1 MHz, the time-domain approach would lead to extremely long simulation times. Moreover, the inclusion of complex permeability with frequency dependence would be more cumbersome.

IV. PARAMETRIZATION IN TERMS OF THE PFN IMPEDANCE

The transverse impedance is of prior interest for beam-dynamics investigations. If a kicker was found to cause a serious beam instability, one would be forced to reduce its coupling impedance to a less harmful value. The well-known, strong dependence of Z_y on the PFN impedance suggests that a PFN modification can reduce this impedance to acceptable values [3–6].

It is therefore of interest to parametrize the transverse kicker impedance in terms of an arbitrary PFN impedance. An approach to achieve this was first proposed by Nassibian and Sacherer [18]. Interpreting the beam current and the kicker-magnet winding as the primary and secondary winding of a transformer, respectively, they developed a simple model for the inductive coupling of the beam to the PFN. Here we follow a very similar route, slightly generalizing their argument.
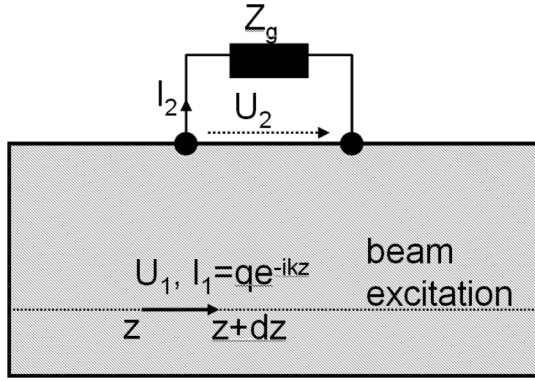
FIG. 1. Black box picture of the kicker module: $U_1 = E_z dz$ is the local voltage between the extremes of an infinitesimal current segment of the twin-wire excitation, with current $I_1 = qe^{-ikz}$. U_2 is the voltage between the PFN kicker plugs. With the lumped PFN impedance Z_g, we have $I_2 = U_2/Z_g$ as the respective current value.

The starting point is to treat the kicker module as a black box, having plugs for the PFN, see Fig. 1. The influence of the PFN is modeled by an attached lumped impedance, as described in Sec. III C. We note that, in using the lumped PFN representation, well-defined voltage, U_2, and current, I_2, between plugs are assumed, implying the absence of wave effects or a TEM-like field distribution between plugs. Furthermore, consider the twin-wire excitation current as being constituted by a large number of infinitesimally short current segments, and take an arbitrary one of those as the excitation depicted in Fig. 1. As the segment is infinitesimal, its local electrical field and current density are equivalent to the local voltage ($U_1 \equiv E_z dz$) and current ($I_1 \equiv qe^{-ikz}$), respectively, (note our convention on units, Sec. II A).

Under these assumptions, the interrelation between the current segment and the lumped PFN is given by a two-by-two impedance matrix, capturing the complexity of the kicker device (black box), i.e.,

$$U_1 = Z_{11}I_1 + Z_{12}I_2 \qquad (11)$$

$$U_2 = Z_{21}I_1 + Z_{22}I_2. \qquad (12)$$

From $U_2 = Z_g I_2$ and Eq. (12), we find

$$I_2 = \frac{Z_{21}}{Z_g - Z_{22}}I_1, \qquad (13)$$

which, in conjunction with Eq. (11), leads to

$$U_1 = \left(Z_{11} + \frac{Z_{12}Z_{21}}{Z_g - Z_{22}}\right)I_1.$$

Using the definitions for U_1 and I_1, this expression can be rewritten as

$$\frac{1}{q}dzE_z e^{ikz} = U_1 I_1^{-1} = Z_{11} + \frac{Z_{12}Z_{21}}{Z_g - Z_{22}}. \qquad (14)$$

Please note that all matrix coefficients but Z_{22} depend on the actual choice of current segment, I_1. Comparing Eq. (14), left-hand side, with Eq. (5), we see that the vertical coupling impedance Z_y can be written as a linear superposition of the terms appearing in Eq. (14), right-hand side, resulting in the parametrization,

$$Z_y(\omega, Z_g) = a(\omega) + \frac{b(\omega)}{Z_g(\omega) + c(\omega)}. \qquad (15)$$

Here, the unknown coefficients $a(\omega)$, $b(\omega)$, and $c(\omega) = -Z_{22}$ have been introduced as an abbreviation for the result of the superposition. Below, we will discuss how to determine them from the simulations. We would like to stress that the value of Eq. (15) is that, knowing $a(\omega)$, $b(\omega)$, and $c(\omega)$, one is able to specify Z_y for arbitrary PFN impedance Z_g. In turn, field simulations can in principle be carried out for a kicker device before the actually used PFN is known. For later usage, we denote the Z_y from the parametrized model $Z_y^{model}(\omega)$ in contrast to $Z_y^{sim}(\omega)$ from Eq. (10).

The second summand of Eq. (15) is similar to the expression originally given by Nassibian and Sacherer with the substitutions

$$b(\omega) \rightarrow \frac{\beta c}{4\omega\Delta^2}\omega^2 M^2, \qquad c(\omega) \rightarrow i\omega L_2, \qquad (16)$$

L_2 and M representing the self-inductance of the kicker winding, and the mutual inductance (twin-wire-beam)-(kicker-winding), respectively. Notice that 2Δ is the spacing of the two wires. The first summand of Eq. (15), $a(\omega)$, is not present in the original work of Nassibian and Sacherer. In their transformer picture of a kicker, $a(\omega)$ would correspond to the self-inductance, L_1, of the twin-wire line, i.e.

$$a(\omega) \rightarrow \frac{\beta c}{4\omega\Delta^2}i\omega L_1. \qquad (17)$$

The equivalent circuit of Nassibian and Sacherer's derivation is shown in Fig. 2 for completeness. Losses inside the
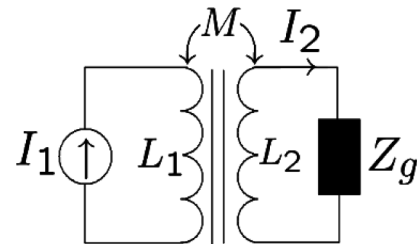
FIG. 2. Equivalent circuit for the Nassibian and Sacherer transformer picture, indicating the mutual inductance, M, between twin-wire line and the kicker winding. L_1 and L_2 denote the self-inductance of the twin-wire line (representing the beam) and the kicker winding, respectively.

ferrite parts would be accounted for by the imaginary part of L_1.

We would like to point out that, while Nassibian and Sacherer's transformer picture, as well as the model advocated in [3], are tied to a certain equivalent circuit, multiple equivalent circuits can be given for the parametrization equation (15) derived here. For instance, the capacitance of the kicker winding and the PFN feedthroughs (which has to be imagined in parallel to Z_g) is covered by Eq. (15). This is obvious from the fact that we used a black-box description of the kicker interior.

Finally, let us address the question of how to compute the coefficients $a(\omega)$, $b(\omega)$, and $c(\omega)$ in the simulations. The approach chosen in this work determines the three complex numbers for each considered frequency point by using three different kicker terminations, i.e.

$$Z_g \in \{0, \infty, 50 \ \Omega\}.$$

From the respective numerical field calculations one obtains $Z_y(\omega, 0 \ \Omega)$, $Z_y(\omega, 50 \ \Omega)$, and $Z_y(\omega, \infty)$, which, in turn, determine the coefficients $a(\omega)$, $b(\omega)$, and $c(\omega)$. Thus, three frequency sweeps are needed within this approach. The application of Eq. (15) is shown below.

V. EXAMPLE: THE SNS KICKER

Among the component devices making a big contribution to the impedance budget of the SNS storage ring, the ferrite kicker magnet [3] represents the most critical one. This device is a window-frame magnet used to deflect the beam vertically by means of a pulsed magnetic field.

In the particular case of the SNS kicker, vertical-impedance measurements were reported by Hahn and Davino using the two-wire technique [3–6] as well as direct impedance measurements [4]. Since details of the measurements as well as dimensions of the kicker have been reported, the SNS kicker is an ideal model for benchmarking the numerical computation of coupling impedances [19]. We further ensured the identity of our kicker model with that used in the measurements by clarifying some details directly with Hahn and Davino.

The schematic view of the SNS kicker in Fig. 3 shows a metallic busbar, i.e., two metallic sheets, inserted in a ferrite frame, which in turn is hitched by a stainless steel frame and a base. The busbar has two end plates in a vertical position, which acts as a capacitor. Figure 3 also shows the vacuum vessel containing the kicker module. The dimensions of this vacuum vessel have been chosen such that possible undesirable effects of the vessel boundaries (vessel walls) on the impedances are negligible. Typical dimensions of the kicker and vacuum vessel are given in Fig. 3.

While the kicker magnet finally built into the SNS electrically connects to the PFN by a feedthrough, leading out of the vacuum vessel, Hahn and Davino have performed impedance measurements on a kicker prototype

where the feedthrough has been neglected. Instead, they have applied different load impedances between the busbar plates directly (short, open, 25 Ω, 50 Ω, 200 Ω). It is this situation that is analyzed in our simulations. As we mentioned in Sec. III C, we simulate the effect of the PFN load by adding an equivalent, lumped impedance at the magnet terminations. In the present case, this amounts to modifying the FIT edge seen in the inset of Fig. 3 (upper panel), according to Eq. (9). The dimensions of the SNS kicker [3,20] can be found in the caption of Fig. 3.

The ferrite type is CMD5005 [21], which is a nickel zinc (NiZn) ferrite with the initial permeability of 1300. In general, the permeability of ferrites is complex and contributes to the formation of eddy currents and hysteresis losses. In order to reduce the loss of beam energy due to these effects (i.e. to reduce *longitudinal* coupling impedance), eddy current stripes are inserted into the ferrite loop [3] as shown in Fig. 3. In the case of the ferrite CMD5005, the log-log behavior of the real and imaginary part of the permeability in the region between 1 and 100 MHz (taken from the manufacturer's data sheet) is rather smooth, which facilitates its interpolation during simulations. On the other hand, the ferrite permittivity in the model was assumed to be $\epsilon_r = 12$ [22] for the range of frequencies considered here. Notice that the value of the permittivity varies with the frequency [22], however, this variation is not larger than 20% for the present range frequencies [22].

A. Comparison with twin-wire measurements

In Fig. 4 the experimentally measured data for Z_y [3,23] are compared with the results from our electromagnetic field simulations, for different external impedances, Z_g. A first observation is that the agreement between measurements and computations is different for different Z_g's. Whereas in the open case ($Z_g = \infty$) the agreement is good, decreasing Z_g steadily leads to larger discrepancies. Second, for given Z_g, the largest deviations arise at high frequencies.

The fact that for the open case, Fig. 4(a), we are able to accurately reproduce the measured resonance (due to the interplay between busbar-plate capacitance and magnet inductance) suggests that our computational model is accurate. We would like to stress that no model adaptation has been done to obtain this agreement.

It is interesting to consider the increasing deviations between simulation and measurement upon decreasing Z_g ($Z_g = 200 \ \Omega$, 50 Ω, short). In the extreme case, $Z_g = 0 \ \Omega$, the coupling between beam (i.e. twin-wire line) and magnet is small as (in the case of a perfectly conducting magnet winding) no magnetic flux may penetrate the loop formed by the winding. Thus, at $Z_g = 0 \ \Omega$, Z_y solely reflects the self-inductance of the twin-wire line. However, as can be seen from the publications on the SNS kicker measurements (e.g. [4], Fig. 11), the calibration of the twin-wire line for measurement is not trivial. As

shown in [4], different strategies for matching the characteristic line impedance to the 50 Ω instrument impedance may lead to different results for Z_y, particularly for frequencies above 20 MHz.

Note that each plot in Fig. 4 contains two data sets obtained from simulations: (i) the directly computed impedances [$Z_y^{\text{sim}}(\omega)$, dots], arising from the solution of the field equations at each frequency point shown, (ii) $Z_y^{\text{model}}(\omega)$ data obtained through the parametrized model of Eq. (15). Some comments on how $Z_y^{\text{model}}(\omega)$ was determined are in order. After Sec. IV, three frequency sweeps allow the construction of the PFN model. Here we have used the data from $Z_y^{\text{sim}}(\omega)$ for $Z_g \in \{0\ \Omega, 50\ \Omega, \infty\}$, see Fig. 5 for the resulting parameters $a(\omega)$, $b(\omega)$, and

$c(\omega)$. Thus, the perfect agreement of $Z_y^{\text{model}}(\omega)$ and $Z_y^{\text{sim}}(\omega)$ seen in Figs. 4(a), 4(c), and 4(d) is to be expected. For Fig. 4(b) ($Z_g = 200\ \Omega$) and Fig. 6 ($Z_g = 25\ \Omega$), however, the model *predicts* the correct $Z_y(\omega)$, as $Z_y^{\text{sim}}(\omega)$ and $Z_y^{\text{model}}(\omega)$ are indistinguishable in the plots.

As mentioned above, multiple equivalent circuits can be given for this parametrized model. The most simple one is shown in Fig. 2, where the unknowns L_1, L_2, and M can be calculated from the coefficients given in Fig. 5 via Eqs. (16) and (17). However, these unknowns turn out to be dependent on frequency in a nontrivial form in the case of the SNS kicker, so no further insight is gained by calculating them. One obvious reason for the shortcoming of the equivalent circuit of Fig. 2 is the presence of the
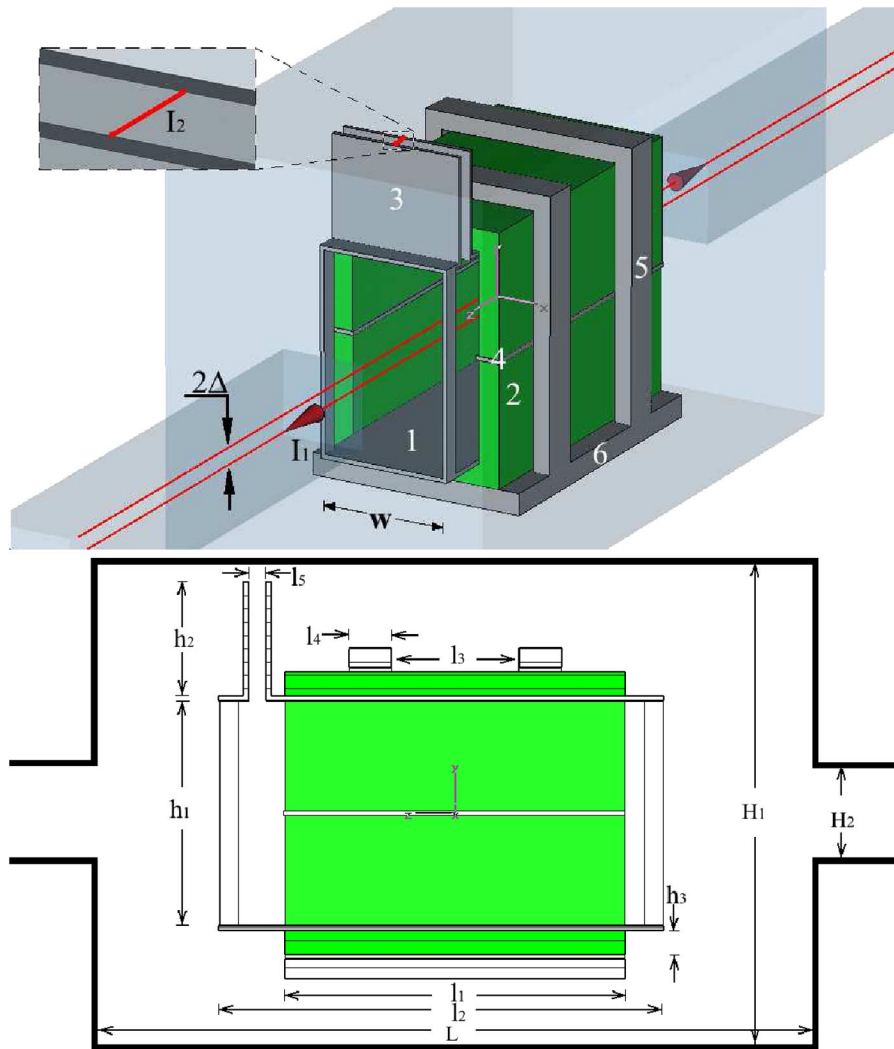
FIG. 3. (Color) Upper panel: schematic view of the SNS kicker with the metallic busbar (1), the ferrite frame (2), the end plates of the busbar (3), the strips (4), a metallic frame (5), and a metallic base (6). In the inset is shown schematically the FIT edge joining the two ends of the end plates. Lower panel: vertical cutting plane yz at $x = 0$ of the kicker magnet. Kicker dimensions: $w = 15.9$ cm, $h_1 = 24.8$ cm, $h_2 = 12$ cm, $h_3 = 2.54$ cm, $l_1 = 36$ cm, $l_2 = 46$ cm, $l_3 = 13$ cm, $l_4 = 4.5$ cm, and $l_5 = l_6 = 2.54$ cm [3,20]. A 0.3 mm-thick vacuum layer between the ferrite frame (2) and the metallic frame (5) and base (6) simulating an insulate layer is taken into account. Typical dimensions of the vacuum vessel: $L = 76$ cm, $H_1 = 53$ cm, and $H_2 = 10$ cm.
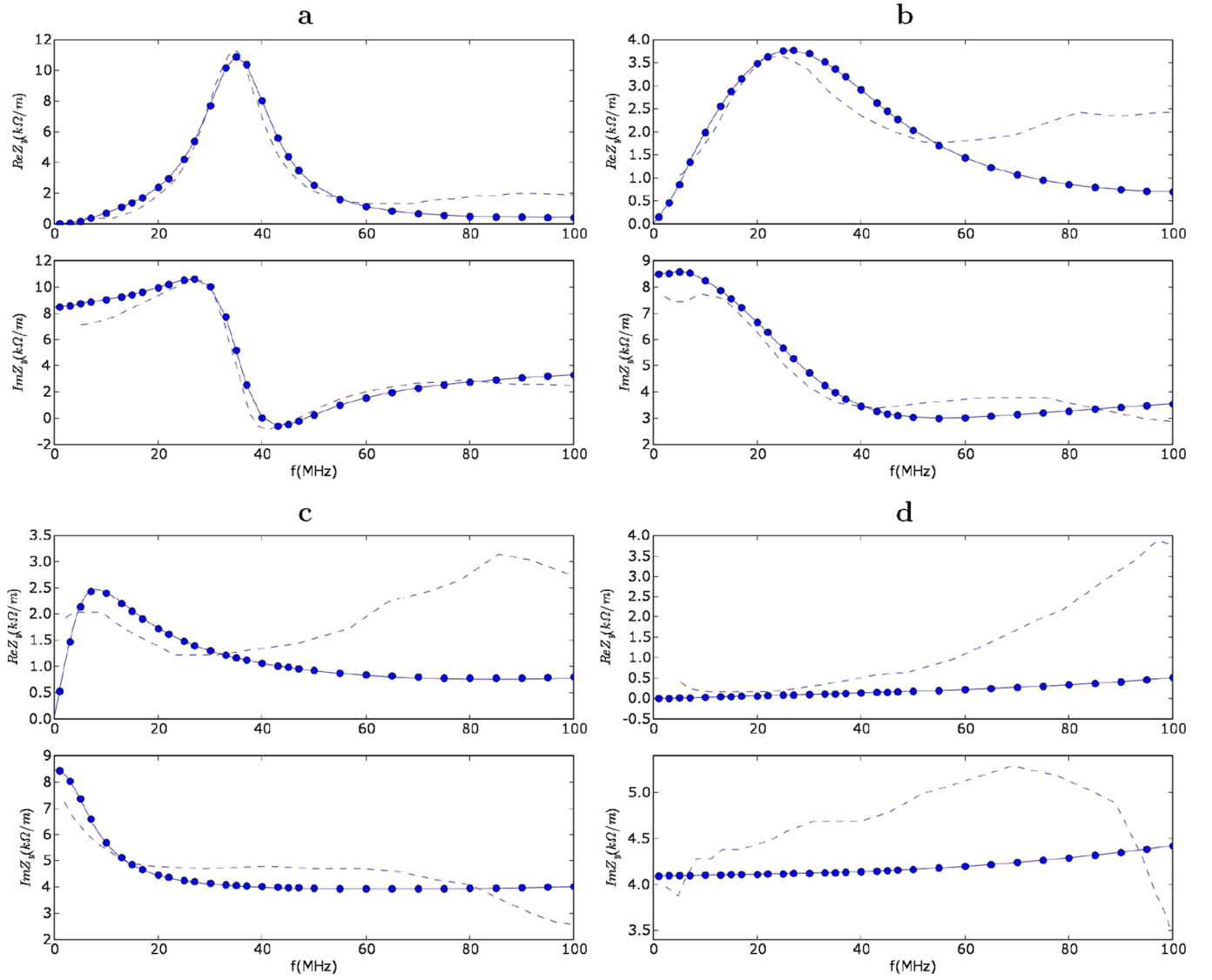
FIG. 4. (Color) Real and imaginary part of Z_y vs frequency for the cases $Z_g = \infty$ (a), 200 Ω (b), 50 Ω (c), and 0 Ω (d). Experimental measurements (dashed lines) [[3] (Fig. 5) and [23] (Fig. 4)] results from numerical field simulations [$Z_y^{\mathrm{sim}}(\omega)$, dots] and estimation from the parametrization [$Z_y^{\mathrm{model}}(\omega)$, solid lines], Eq. (15), are plotted together for comparison.

capacitance between busbar plates, which appears in parallel to Z_g. Moreover, due to the losses inside the ferrite parts, L_1, L_2, and M contain a frequency-dependent imaginary part. Given the simulation results of Fig. 5, it would be possible to determine the parameters for a modified equivalent circuit which includes these effects. If, however, the details of the kicker interior (concrete values of L_1, L_2, M, C_{plates}, ferrite losses, etc.) are of no direct interest to the analysis, it is more convenient to work with the parametrized model. The latter is valid for any component, due to the use of the black-box description.

Another motivation for working with the parametrized model is that the curves $a(\omega)$, $b(\omega)$, and $c(\omega)$ are rather smooth. Thus, only a relatively sparse set of frequency points $\{\omega_i\}$ needs to be considered for explicit simulation

[i.e. computation of $Z_y^{\mathrm{sim}}(\omega, Z_g)$ for $\omega \in \{\omega_i\}$, $Z_g \in \{0\ \Omega, 50\ \Omega, \infty\}$]. In contrast, explicitly computing $Z_y^{\mathrm{sim}}(\omega)$ for an actual PFN impedance typically requires a much denser frequency sampling; see the next section for an illustration of this statement.

B. Comparison with direct measurements

In the case of low frequencies (< 10 MHz), the two-wire method is not suitable for measuring transversal coupling impedances due to its small signal-to-noise ratio [4]. For this range of frequencies so-called *direct* coupling impedance measurements [24] were performed at the SNS kicker [4]. By probing the kicker terminations (here: the end plates of the busbar) with a network analyzer, the
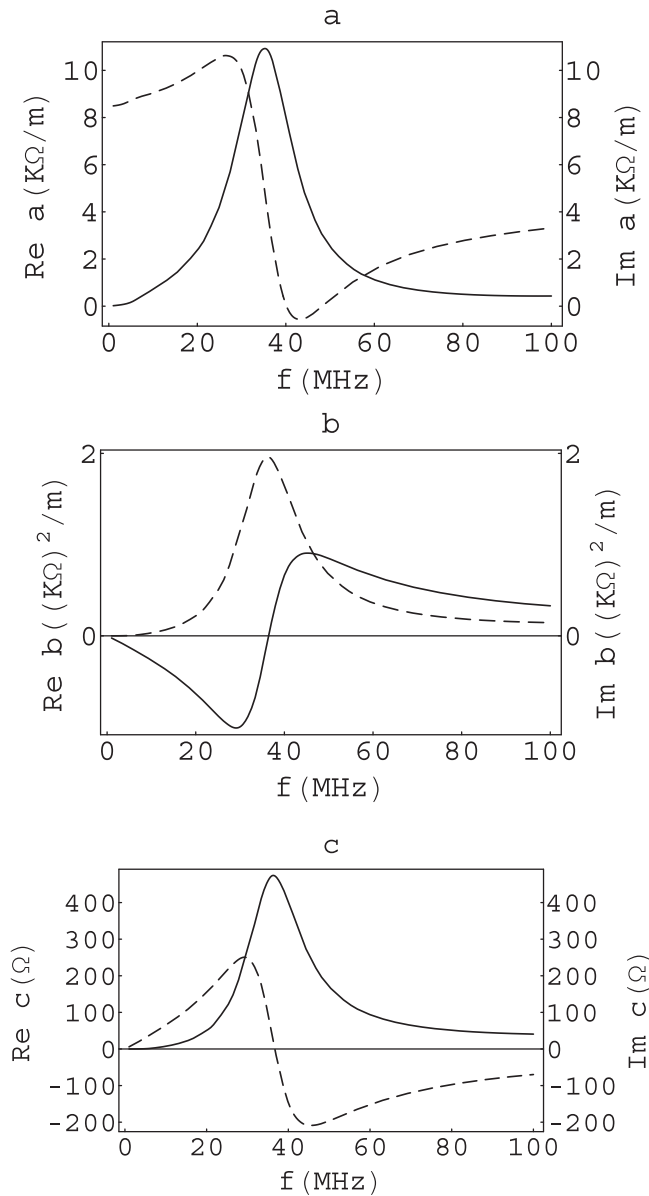
FIG. 5.   Real (solid line) and imaginary (dashed line) parts of the parameters $a(\omega)$, $b(\omega)$, and $c(\omega)$ vs frequency.

FIG. 6. (Color) Real and imaginary part of Z_y vs frequency for $Z_g = 25\ \Omega$: direct measurements (dot-dashed line, computed from Z^D in [4], Fig. 15), two-wire measurements (dashed line) [3], simulations [$Z_y^{\text{sim}}(\omega)$, dots], and prediction from the parametrization [$Z_y^{\text{model}}(\omega)$, solid line].

magnet inductance (L_2) can be determined directly. For a window-frame kicker, after the Nassibian and Sacherer approach [18], one is able to express the beam-to-magnet coupling (i.e. the mutual inductance M) by an approximate analytical formula. Thus, after Eqs. (15) and (16), the transverse kicker impedance can be computed if $a(\omega)$ is neglected. A similar approach has been used by Hahn [4], leading to the expression

$$Z_y^{\text{dir}}(\omega) = \frac{\beta c}{4\omega\Delta^2} Z_D(\omega), \qquad (18)$$

where $Z_D(\omega)$ is the impedance seen at the kicker plugs.

One advantage of the direct measurement technique is that the insertion and calibration of the twin-wire line are

not needed. Thus, direct measurements can also be performed with devices already mounted in an accelerator [24] as long as (i) the kicker plugs are accessible and (ii) one is dealing with the transverse coupling impedance *along the kick direction* (here, the vertical direction). The disadvantage of the direct method is that the self-inductance L_1 of the twin-wire line (due to the so-called "uncoupled" flux [3]) is not accessible.

We consider the direct measurement of the vertical impedance for the case $Z_g = 25\ \Omega$ [4], see Fig. 6, comparing it with the results from the twin-wire measurements. Concerning ReZ_y below 30 MHz, we observe an agreement of the two measurement methods within 30%, whereas much larger deviations are found above 30 MHz. For ImZ_y, the twin-wire curve is offset by approximately $-4.1\ \text{k}\Omega/\text{m}$ with respect to the twin-wire curve, which, as explained above, can be attributed to the missing uncoupled flux in the direct method. Additionally, an oscillation in the twin-wire ImZ_y is observed at high frequencies that is not present in the direct results.

Interestingly, our simulation results, also shown in Fig. 6, agree very well with the direct measurements over the complete frequency range considered. (For ImZ_y, a nearly constant vertical offset of approximately $-4.1\ \text{k}\Omega/\text{m}$ is found between direct simulation and measurement results.)

We note besides that in the "short" case [Fig. 4(d)] Im$Z_y(\omega \to 0)$ exactly equals the observed offset between curves.

A further comparison between direct measurements and simulations is shown in Fig. 7. In this case, the SNS kicker prototype has been connected to the actual PFN device via
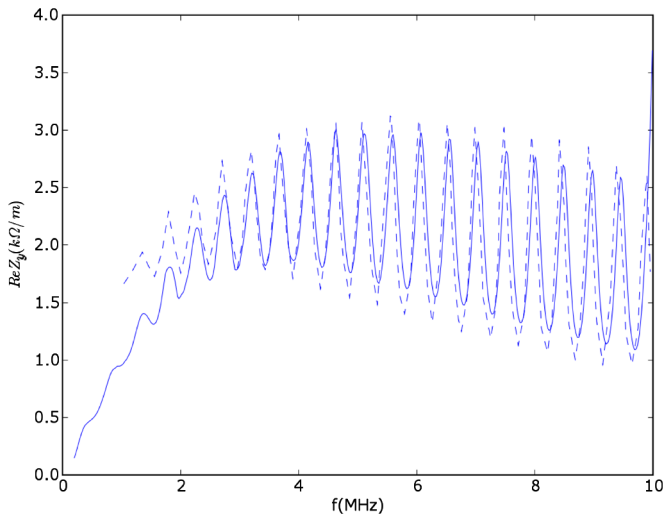
FIG. 7. (Color) Real part of Z_y vs frequency of the SNS kicker prototype with the actual PFN, connected to the kicker by 200 m long 50 Ω cables. Dashed line: direct measurements [4], Fig. 17 (''no screen''). Solid line: simulation results obtained from the parametrization, Eq. (15), see text.

a feedthrough and two 200 m long, 50 Ω coaxial cables [4]. The cables are in parallel to match the nominal 25 Ω output impedance of the PFN device. Thus, the value of Z_g as used throughout this paper is determined by the series connection of the feedthrough, the transmission line formed by the cables and the PFN device. Because of small, frequency-dependent deviations of the PFN output impedance from 25 Ω, oscillations of $Z_g(\omega)$ arise. The footprint of these oscillations can be seen in the measurement data of Z_y, Fig. 7.

In order to compute Z_y from the simulation results condensed in the parametrized model [Eq. (15), data of Fig. 5], $Z_g(\omega)$ needs to be known. First, for simplicity, we have neglected the contribution of the feedthrough. Second, the output impedance of the PFN device was taken from the measurements of Hahn [4], Fig. 16. Third, $Z_g(\omega)$ was computed via transmission line theory. Using Eq. (15), we then computed $Z_y(\omega)$, see Fig. 7 for the result. Again, a good agreement between direct measurements and simulations can be observed.

VI. SUMMARY AND CONCLUSIONS

We have reported on our numerical framework for computing coupling impedances of fast kicker modules. In addition to the advantage that no prototyping is required, the presented simulation approach is able to readily describe the special kind of excitation current due to the beam (including its boundaries). Since one goal of the work presented here was to demonstrate the compatibility of simulation results with those of measurements, we have considered the case of vertical impedances of the SNS

extraction kicker, for which detailed experimental results had been published.

After a brief review of the theoretical foundations of coupling impedances and a description of our algorithm, we have developed a parametrized model for the interaction of the kicker with the pulse-forming network. Using this model essentially offers two advantages: (i) after setting up the parameters [$a(\omega)$, $b(\omega)$, and $c(\omega)$], one can experiment with different PFN versions and determine their footprint on the coupling impedance, (ii) computing the model by three frequency sweeps (here $Z_g \in \{0\ \Omega, 50\ \Omega, \infty\}$) can be more efficient than directly considering the actual PFN impedance in the simulations (compare Fig. 7). Despite the simplicity of the black-box model, the parametrization fully captures the physics of the beam-PFN coupling. It can thus serve as a cross-checking tool for simulations or measurements, in case more than three frequency sweeps are available [compare Figs. 4(d) and 6].

As described in Sec. II B, the computations are based on the twin-wire approximation equation (6) of the beam current, which becomes more accurate the finer the numerical mesh (Δ can be set to the size of a single transversal mesh step).

Finally, a good agreement is observed between numerical and experimental results for frequencies below 60 MHz, supporting the viability of the work presented here. For higher frequencies, a discrepancy is observed which is still an object of further research.

[1] B. W. Zotter and S. A. Kheifets, *Impedances and Wakes in High Energy Particle Accelerators* (World Scientific, Singapore, 1998).

[2] J. Wei *et al.*, Phys. Rev. ST Accel. Beams **3**, 080101 (2000).

[3] D. Davino and H. Hahn, Phys. Rev. ST Accel. Beams **6**, 012001 (2003).

[4] H. Hahn, Phys. Rev. ST Accel. Beams **7**, 103501 (2004).

[5] D. Davino, H. Hahn, and Y. Y. Lee, *8th European Particle Accelerator Conference EPAC, Paris, France*, 2002, p. 1467.

[6] D. Davino and H. Hahn, BNL/SNS Technical Note No. 102, 2001.

[7] R. L. Gluckstern, CERN Report No. 2000-011, 2000, http://www.slac.stanford.edu/spires/hep/browse/.

[8] T. Weiland, Int. J. Electron. Commun. (AEÜ) **31**, 116 (1977).

[9] T. Weiland, Part. Accel. **15**, 245 (1984).

B. DOLIWA, E. ARÉVALO, AND T. WEILAND

Phys. Rev. ST Accel. Beams **10,** 102001 (2007)

[10] B. Doliwa, H. De Gersem, and T. Weiland, Proceedings of the 2005 Particle Accelerator Conference (PAC), Knoxville, Tennessee, USA, 2005, p. 1820.

[11] B. Doliwa and T. Weiland, Proceedings of the 9th International Computational Accelerator Physics Conference (ICAP 2006), Chamonix, France, 2006, p. 277.

[12] B. Doliwa, H. De Gersem, and T. Weiland, Proceedings of EPAC 2006, Edinburgh, Scotland, 2006, p. 2179.

[13] M. Clemens and T. Weiland, Prog. Electromagn. Res. **32**, 65 (2001).

[14] M. Balk, R. Schuhmann, and T. Weiland, Proceedings of IEEE AP-S/URSI 2003, Columbus, Ohio, 2003, p. 367.

[15] CST GmbH. Bad Nauheimer Str. 19, 64289 Darmstadt.

[16] http://software.sandia.gov/Trilinos.

[17] E. Gjonaj, X. Dong, R. Hampel, M. Kärkkäinen, T. Lau, W. F. O. Müller, and T. Weiland, Proceedings of the 9th International Computational Accelerator Physics Conference (ICAP 2006), 2006, p. 29.

[18] G. Nassibian and F. Sacherer, Nucl. Instrum. Methods **159**, 21 (1979).

[19] E. Arévalo, B. Doliwa, and T. Weiland, Proceedings of the 9th International Computational Accelerator Physics Conference (ICAP 2006), Chamonix, France, 2006, p. 128.

[20] H. Hahn and D. Davino (private communication).

[21] National Magnetics Group. 1210 Win Drive, Bethlehem, Pennsylvania 18017-7061, USA, http://www.magneticsgroup.com/.

[22] C. C. Jensen and J. A. Dinkel, IEEE Trans. Magn. **31**, 804 (1995).

[23] D. Davino and H. Hahn, BNL/SNS Technical Note No. 102, 2001.

[24] U. Blell, Proceedings of the Particle Accelerator Conference, Vancouver, Canada, 1997, p. 1727.